BRIEF REPORT

Iterative immunostaining combined with expansion microscopy and image processing reveals nanoscopic network organization of nuclear lamina

Elina Mäntylä,[a*] Toni Montonen,[a*] Lucio Azzari,[b] Salla Mattola,[c] Markus Hannula,[a] Maija Vihinen-Ranta,[c] Jari Hyttinen,[a] Minnamari Vippola, Alessandro Foi,[d] Soile Nymark,[a] Teemu O. Ihalainen[a]

BioMediTech, Faculty of Medicine and Health Technology, Tampere University, Tampere, Finland[a]; Tampere Microscopy Center (TMC), Tampere University, Tampere, Finland[b]; Department of Biological and Environmental Science and Nanoscience Center, University of Jyväskylä, Jyväskylä, Finland[c]; Faculty of Information Technology and Communication Sciences, Computing Sciences, Tampere University, Tampere, Finland[d]

*Equal contribution
#Address correspondence to Teemu Ihalainen, teemu.ihalainen@tuni.fi

Address: BioMediTech, Faculty of Medicine and Health Technology,
Tampere, University, Tampere, Finland. Arvo Ylpön katu 34, 33520 Tampere, Finland
Phone: +358 50 3187 202

Characters (without spaces): 20 000
Running head: IT-IF IN EXPANSION MICROSCOPY OF LAMINS

Abbreviations:

ExM	Expansion microscopy
FWHM	Full width at half maximum
HSV-1	Herpes simplex virus 1
IT-IF	Iterative indirect immunofluorescence staining
LA/C-C	Lamin A/C C-terminus
LA/C-N	Lamin A/C N-terminus

LA/C-rod	Lamin A/C rod-domain
NE	Nuclear envelope
PAA	Polyacrylamide
SBR	Signal-to-background -ratio
SIM	Structured illumination microscopy
SR-SIM	Super-resolution structured illumination microscopy

Abstract

Investigation of nuclear lamina architecture relies on super-resolved microscopy. However, epitope accessibility, labeling density, and detection precision of individual molecules poses challenges within the molecularly crowded nucleus. We developed iterative indirect immunofluorescence (IT–IF) staining approach combined with expansion microscopy (ExM) and structured illumination microscopy improving super-resolution microscopy of subnuclear nanostructures like lamins. First, we prove that ExM is applicable in analyzing highly compacted nuclear multiprotein complexes such as viral capsids. Second, we provide technical ExM improvements, including 3D-printed gel casting equipment. Third, we show that in comparison to conventional immunostaining, IT-IF results in a higher signal-to-background – ratio (SBR) and mean fluorescence intensity and use structured illumination microscopy and ExM to critically point out that iterative immunostaining results in improved target labeling density, benefiting the structural analyses via ExM. Lastly, we develop a signal processing pipeline for noise estimation, denoising, and deblurring in the analysis of lamin networks and provide this platform to the microscopy imaging research community. Our work reveals the potential of signal-resolved IT–IF in super-resolution imaging of lamin network organization - a prerequisite for studying intranuclear structural co-regulation of cell function and fate. (Words: 187)

Introduction

Nuclear envelope (NE) is underlined by a tight proteinaceous network called nuclear lamina (NL). The NL is formed of type V intermediate filaments called A and B-type lamins and associated proteins (Schirmer et al., 2003). The A- and B-type lamins form separate layers with the latter situated closer to the NE (Figueiras et al., 2019). Together, lamins form approximately a 14 nm-thick layer less than one-tenth of the resolution of the diffraction-limited fluorescence microscopy (Pawley, 2006). The NL is necessary for the nuclear mechanical stability (Dahl et al., 2004) and responds to mechanical cues (Ankam et al., 2018). It has pivotal roles in

regulating genome organization and gene expression (Brueckner et al., 2020) by tethering chromatin (Robson et al., 2016). The NL –chromatin interaction is highly dynamic (Dixon et al., 2015), and changes, e.g., during differentiation (Cavalli and Misteli, 2013; Fortin and Hansen, 2015). To study the role of lamins in the co-regulation of the genome, a detailed understanding of the NL organization is required. Hence, super-resolution imaging of the NL has gained significant interest.

Expansion microscopy (ExM) is a tempting super-resolution microscopy technique enabling the detection of complex nanostructures by using fluorescence-based imaging modalities, e.g., selective plane illumination microscopy or laser scanning confocal microscopy (LSCM). ExM is based on isotropic enlargement of the sample via 4X – 10X expandable hydrogel. However, this expansion dilutes the fluorophores in the sample reducing the resulting image brightness. The dilution scales to the third power of the (linear) expansion factor and thus even 4X expansion can lead to a 64X reduction of the fluorescent signal. To compensate for the dilution, high-quality imaging with ExM, as with other super-resolution methods, requires high-density labeling of the targets (Dankovich and Rizzoli, 2021). However, conventional indirect immunostaining can be insufficient and include non-specific binding, which causes off-target staining of the background and consequent reduction in the image signal-to-background ratio (SBR) and contrast (Lau et al., 2012; Whelan and Bell, 2015). Furthermore, the accessibility of the target protein epitopes can drastically affect the quality of the data (Schnell et al., 2012). The low signal quality in ExM can be improved by post-processing the data by denoising (Chen et al., 2021), deconvolution (Ikoma et al., 2018), or by a combination of both.

We present an improved ExM method utilizing iterative immunofluorescence (IT-IF) staining and image processing further facilitating detection and quantitative analysis in super-resolution microscopy of the nucleus. We provide free image processing tools specifically designed to perform noise reduction on LSCM data. We prove that IT-IF leads to increased signal intensity without compromising the SBR, advancing super-resolution imaging of highly compact intranuclear structures. Finally, we exploit these methods to reveal nanoscopic structural details of NL network organization.

Results and discussion

ExM enables high-resolution imaging of highly compacted nuclear multiprotein complexes but compromises fluorescence intensity and signal-to-background -ratio

ExM allows super-resolution imaging of biological specimens using standard fluorescence microscopy systems. It is based on the isotropic physical expansion of the sample, leading to a corresponding increase in the spatial resolution (Tillberg et al., 2016). Here, fixed and immunostained samples are treated with a cross-linker, embedded into polyacrylamide (PAA) hydrogel, homogenized, and osmotically expanded in water (Figure 1A). We investigated if ExM results in isotropic expansion of rigid and compact nano-scale structures within the nucleus. For this, we used HSV-1 -infected fibroblasts (12 h post-infection, multiplicity of infection 5) (Figure 1B). HSV-1 naturally targets nuclei for replication producing 125 nm-wide self-assembling progeny capsids in the nucleoplasm (Newcomb et al., 1996; Ojala et al., 2000; Baines, 2011). After immunostaining with a viral capsid protein 5 (VP5) antibody (Ab), the samples were prepared for ExM (n=2, expansion factor ~4), imaged with LSCM, and deconvoluted. From images 12 intranuclear anti-VP5 labeled ring-like viral capsids were extracted, aligned, averaged, and their mean diameter was measured as the peak-to-peak distance from the normalized intensity profile. The mean capsid size was 125.4 nm correlating well with that of the native virus (Figure 1B). This is in good agreement with previous studies, where super-resolution STORM-imaging of HSV-1 resulted in approximately 133 nm diameter for the tegument layer outside the capsid (Laine et al., 2015). Thus, the assay showed successful isotropic expansion of the intranuclear viral capsids, indicating ExM suitability for super-resolution imaging of compact intranuclear objects (Gao et al., 2021).

We then compared the performances of LSCM, SR-SIM, and ExM+LSCM in imaging of NL (Figure 1C). Previous cryo-electron tomography and fluorescence lifetime –based studies on the molecular architecture of the NL (~14 nm) have shown that A-type lamins A and C (LA/C) form a separated network of ~10 nm in thicknesses (Turgay et al., 2017; Figueiras et al., 2019). Thus, the NL falls beyond the diffraction-limited resolution of a confocal microscope and presents a good intranuclear target for comparison of different imaging modalities. Here, cells were stained with a mouse monoclonal Ab (mMAb) targeting the lamin A/C rod-domain (LA/C-rod) and mounted for high-resolution LSCM and SR-SIM (n=2). Consequently, LA/C-rod –stained ExM samples were prepared from replicate samples by crosslinking and embedding into the PAA gel using novel in-house 3D-printed spacers designed to ensure constant sample gel thickness and diameter (Supplemental Figure 1, A and

B). After homogenization, the samples were expanded in water (expansion factor ~4.4, n=2). Following imaging with LSCM, SR-SIM, and ExM+LSCM, the width of the LA/C rim was determined from the middle section of the nucleus by measuring the full width at half maximum (FWHM) (Figure 1C). The LSCM yielded the thickest lamina with a mean thickness of 273.0 nm ± 0.04 nm. The SR-SIM improved the resolution, and the lamina thickness was 182.0 nm ± 0.4 nm. The ExM provided the highest resolution, with a lamina thickness of 110.0 nm ± 0.4 nm. LSCM and SR-SIM showed surprisingly mediocre performance and the resulting thicknesses were much larger than the theoretical diffraction limit. The results indicate that the ExM yielded considerably improved resolution (smaller FWHM of the NL) in comparison to LSCM or SR-SIM when imaging intranuclear structures.

Ab concentrations used in ExM are typically higher than those used in conventional immunostaining protocols because the ExM dilutes fluorescence signal by a factor of expansion in the power of three (Truckenbrodt et al., 2019). To demonstrate this effect, we next prepared pre- and post-expansion samples from cells stably over expressing histone H2B-EGFP. In addition, to visualize the effect of expansion on the Ab-derived intensity, replicate samples were stained with an Ab recognizing LA/C N-terminus (LA/C-N) using standard Ab concentrations. To study the effects of high Ab concentration on the intensity and the SBR, additional samples were prepared with 4X higher primary (1°) and secondary (2°) Ab concentrations. The fluorescence intensity and the mean SBR were determined with identical LSCM imaging settings before and after the expansion (expansion factor 4.4; n=2). Of note, the SBR here described the ratio of background-corrected nuclear intensity to the intensity resulting from off-target and background staining measured from the cytoplasm.

The H2B-EGFP intensity was found to be 1620 ± 140 (a.u.) (mean ± standard deviation, SD) before the expansion but was significantly reduced by 91 % to 153 ± 41 a.u. in expansion (n=2). Consequently, the SBR before the expansion was 14.7 but decreased by 88 % to 1.7 after the expansion (Figure 1, D and E). For LA/C-N (n=2), the intensity was 257 ± 53 a.u. before the expansion reducing to 183 ± 81 a.u. after the expansion showing that the expansion led to a ~30 % decrease in the intensity. Consequently, the LA/C-N expansion led to a 58 % decrease in the mean SBR (from SBR of 3.1 to 1.3) (Figure 1E). The analysis of samples containing 4X LA/C-N Ab (n=2) concentrations showed that the intensities were almost 4X higher in comparison to that acquired with 1X concentrations. Specifically, the quantification indicated that the LA/C-N intensity before the expansion was 950 ± 150 a.u. and reduced to 435 ± 72 a.u. following the expansion meaning a 54 % decrease in intensity. Also, the expansion led to a 71 % decrease in the SBR from 6.6 to 1.9 (Figure 1E).

Together, the results indicate that ExM enables imaging of highly compacted nuclear protein assemblies. Also, the results describe the reduction in intensity and SBR in ExM imaging demonstrating that the ExM decreases signal intensity due to dilution of the fluorophores within the sample (Truckenbrodt et al., 2018; Wassie et al., 2019; Gaudreau-Lapierre et al., 2021). The caveat here is that proper imaging of samples like these requires longer acquisition times and higher detector gains leading to increased noise and photobleaching. However, our results show that increasing the Ab concentration solely does not rescue the image quality. As our analysis of the pre-and post-ExM gel-embedded samples critically showed, the labeling method requires further developed to counteract the resulting decrease in sample fluorescent intensity and signal quality.

Altering concentration-ratio of primary and secondary Abs does not improve fluorescence signal intensity or signal-to-background ratio

We then sought to study whether sample intensity or SBR could be improved by changing the ratio of 1° and 2° Abs. For this, we used either traditional (1X) or increased (4X) 1° or 2°Ab concentrations while simultaneously using the 1X concentration of the other, respectively (n=2; see also Supplemental Figure 2 for histone H3 Ab).

The analysis of samples stained with traditional 1X concentrations of both 1°Ab (LA/C-N) and 2°Abs and normalized to DAPI signal showed a mean nuclear fluorescence intensity (n=2) of 0.6 ± 0.07 a.u. with a mean SBR of 8.6 ± 3.1 (Figure 2A-C). In comparison, using 4X 1° Ab with 1X 2° Ab or 1X 1° Ab with 4X 2° Ab did significantly affect neither the fluorescence intensity (0.6 ± 0.19 and 0.7 ± 0.25 a.u., respectively) nor the mean SBR (6.6 ± 2.7 and 7.1 ± 3.9, respectively) (Figure 2A-C). Comparable results were obtained using histone H3 Ab labeling (Supplemental Figure 2A-F). To analyze further, the labeling density and efficacy in the concentration-enhanced samples were imaged with SIM (Figure 2, D and E) and ExM (Figure 2, F and G) (see also Supplemental Figure 2, G and H for H3 Ab). In comparison to the LSCM, SIM produced a more resolved lamin network (Figure 2, D and E) highlighting the significance of super-resolution imaging in studying lamins. However, the treatments did not influence the SIM exposure time indicating equal intensities between the samples. Finally, ExM-LSCM imaging revealed that an increased concentration of the primary Ab (4X 1° Ab) was required to obtain a better signal (Figure 2F, panel iv). The increase in Ab abundance resulted in more dense staining and visually improved detection of filamentous-like structures within the sample. However, increased background staining was also observed (Figure 2G,

panel iv). In comparison, the samples treated with 4X 2° Ab were dim (Figure 2F, panel v), and the labeling density was low (Figure 2G, panel v).

Together, these results show that increasing the 1° or 2°Ab concentrations alone is insufficient to improve the image quality in SIM and ExM-LSCM. However, increasing the 1° Ab concentration might improve the intensity suggestively via increasing labeling density benefiting ExM-LSCM. However, it needs to be highlighted that optimal final concentration is a balance between the affinity of the antibody for its targeted epitope and its non-specific binding.

Iterative indirect immunostaining improves fluorescence intensity while preserving a high signal-to-background ratio

To improve the staining process by increasing Ab abundance within the sample, iterative indirect immunostaining (IT-IF) was developed. Here, subsequent immunostaining cycles were performed four times, omitting the blocking step in the last three. Each round involved four steps: i) permeabilization followed by ii) incubation with a 1° Ab with uniquely determined optimal concentrations (referred here as 1X), iii) washing, and finally, iv) 2° Ab incubation by using optimized concentrations followed by LSCM imaging.

First, to ensure that the detection conditions did not interfere with the analysis of weak fluorescence intensities, the effects of detector voltage and laser power on the linearity of the detection were determined (Supplemental Figure 3). For the iteration experiments, the nuclear lamin A/C was stained with either monoclonal Abs targeting the protein N- (LA/C-N, PFA and MetOH fixed) or C-terminus (LA/C-C, PFA fixed), or the full-length protein (LA/C-rod, PFA fixed) Ab, or a polyclonal Ab (pLA/C, MetOH fixed) (Figure 3). Histone H3 and H3K9me3 Abs and fluorophore-conjugated phalloidin against F-actin were used as controls (Supplemental Figure 4).

The analyses of normalized intensity values (see Materials and Methods) showed that the total fluorescence intensity was increased due to the iterative staining with all tested Abs but not with the phalloidin (Figure 3, Supplemental Figure 4). For the lamin stained samples, the iterations increased the background-corrected mean fluorescence intensity of LA/C-N by ~2.7 fold in PFA-fixed (Figure 3A) and by ~3.6 fold in MetOH-fixed samples (Figure 3B). Similarly, the intensities were increased in PFA-fixed LA/C-C (by ~1.9 fold) and LA/C-rod (~4.4 fold) stained, and MetOH-fixed pLA/C (by ~8.6 fold) stained samples (Figure 3, C-F). Consequently, the background intensity (I_B) was increased by ~2.4 fold for PFA-fixed LA/C-

N, by ~2.2 fold for MetOH-fixed LA/C-N, by ~2.5 fold for PFA-fixed LA/C-C, by ~7.4 fold for PFA-fixed LA/C-rod, and lastly, by ~8.6 fold for MetOH-fixed pLA/C (Figure 3, A-F). However, even after four iterations, the background staining interfered neither with the detection nor the visual interpretation of the results with the studied Abs. This was apparent, especially from the quantitated SBRs. Specifically, the mean background-corrected SBRs after the first iteration were ~28.80 for LA/C-N (PFA), ~31.42 for LA/C-N (MetOH), ~16.26 for LA/C-C (PFA), ~10.37 for LA/C-rod (PFA), and ~3.73 for pLA/C (MetOH) (Figure 3, A-E, right panels).

To analyze and compare the SBRs in the following iterations, the SBRs from the first iteration were normalized to 1. Next, the SBRs for the following iterations were calculated and normalized to iteration 1) (Figure 3, A-E, right panels). After the four iterations, the SBR in LA/C-N (PFA) staining remained nearly unaltered (from 1 to 1.26, statistically non-significant, ns, $p>0.05$). In contrast, in MetOH fixed LA/C-N samples, the SBR was increased by each iteration and was significantly improved after the fourth iteration (from 1 to 1.7, ***$p<0.01$). For the LA/C-C (PFA), the SBR also remained nearly similar during the first three iterations but slightly decreased after the fourth (from 1 to 0.78, *$p<0.05$). In LA/C-rod (PFA) treated samples, the SBR was significantly lowered after the four iterations (from 1 to 0.592, ****$p<0.001$). This suggested that the polyclonal binding property of the Ab might have negatively affected the SBR during the iterations. Lastly, the SBR of ~1.0 was well retained in all four pLA/C (MetOH) iterations ($p>0.05$). Of note, the IT-IF improved the SBRs of both histone Abs (H3 (PFA) and H3K9me3 (MetOH)) but did not affect that of phalloidin (PFA, Supplemental Figure 4). These analyses show that the iterations increase the intensity of the samples and maintain the SBR depending on the Ab specificity. Thus, the absolute difference between the signal and background increased considerably.

It was then sought to determine how the iterations affected the super-resolution imaging of the samples. To this end, SIM and ExM-LSCM imaging after the first and fourth iterations were done. The experiment showed that the iterations enabled SIM imaging with shorter exposure times as the sample intensity was increased. Also, the structural details, including the NL at the nuclear rim, appeared more uniform (Figure 4, A and B). Similarly, the ExM-LSCM imaging showed that the iterations seemed to increase the sample intensity, and notably, the lamin organization appeared more evident and visible (Figure 4, C and D). These results indicated that iteration-enhanced labeling density within the sample leads to enhanced intensity and contrast.

Together, these results show that the IT-IF improves the sample imaging properties. Specifically, the signal intensity was increased without compromising the SBR. While using either low concentrations or low-affinity Abs might reduce background, it causes low signal intensity to be lost in the noise.

IT-IF with modeling-based denoising improves quantitative lamin network detection

We sought to determine whether the IT-IF improves the analysis of NL structural organization. For this, multicolor detection of the four iterations with LA/C-N was done by using Alexa 647-2°Ab in first and second iterations, and Alexa 568- and Alexa 488-2°Abs in third and fourth iterations, respectively (Figure 5, A and B). This multicolor staining enabled the analysis of labeling patterns after each iteration (Figure 5C) and analysis of their spatial correlations (Figure 5D).

The multicolor analysis revealed that each iteration improved the detection efficiency of lamin by enhancing the Ab occupancy through binding to new targets not bound during preceding iterations (Figure 5, A and B). This was confirmed by intensity line profile analysis showing iteration-specific intensity peaks, and by Pearson´s correlation coefficient (PCC) analysis where the correlation between the stainings was reasonably strong, but weakened significantly during the consecutive iterations (Figure 5, C and D, n=2). The PCC after the two first iterations in comparison to the third was found to be 0.839 ± 0.037, while being significantly lowered to 0.794 ± 0.067 in comparison to that of the fourth iteration (**$p<0.01$, Student´s paired T-test, n=3) (Figure 5D). These results suggested that each consecutive iteration produced new and additional Ab binding along the lamins.

Finally, the power of IT-IF in the detection of lamin network organization was studied by comparing 1°Ab concentration -enhanced (4X 1° Ab and 1X 2° Ab) and four times iterated LA/C-N –stained IT-IF samples by using ExM (n=2). Again, the measured data featured a low signal quality highlighting the need for solutions to get a faithful estimation of the clean signal for reliable quantification of the network properties. For this, we developed a signal-processing software for Noise Estimation, Denoising, and Deblurring [https://github.com/lucioazzari/NoiseEstimationDenoisingDeblurring] that automatically estimates the noise and performs signal reconstruction intended as denoising and deblurring (see Materials and Methods for detailed description for the pipeline). After processing the images, we observed that in comparison to the concentration enhanced-samples, the four-time iterated IT-IF samples displayed a clear improvement in the overall signal quality showing

well-defined lamin structures. Specifically, IT-IF-ExM enabled detailed quantitative analysis of the lamin network architecture. The physical properties of the LA/C-N –stained lamins were determined by analyzing the lamin segment length and width. The analysis showed equal lamin segment length and radius for both 4X 1°Ab/1X 2°Ab and IT-IF samples (0.16±0.009 µm and 0.15±0.004 µm; and 0.06±0.00 µm and 0.06±0.00 µm, respectively) suggesting that the two different approaches did not affect the physical properties of the lamin segments (Figure 5 E-G). The LA/C network properties were then analyzed by quantifying the numbers of total, terminating, and branching nodes connecting the observed lamin structures, and lamin segments. The quantification indicated significantly higher numbers of total and branching nodes in the four times iterated IT-IF samples (519 nodes, ***p=0.001; and 274 nodes, ***p<0.0001, 2way ANOVA multiple comparisons tests) in comparison to that in the concentration enhanced sample (449 total nodes and 181 branching nodes) (Figure 5H). There were no differences in the number of terminal nodes between the samples. In addition, the analysis indicated a significant (***p<0.0001 2way ANOVA multiple comparisons test) increase in the number of lamin segments in the IT-IF sample (565 segments) in comparison to the concentration-enhanced sample (429 segments) (Figure 5H). Together, the results indicate that the iterative pre-ExM method IT-IF improved the ExM detection and quantification of the NL structural organization.

Overall, the findings of this study indicate that IT-IF combined with ExM and signal processing advance the detection of nuclear lamin structure in the super-resolution scale by providing high labeling density, intensity, and uncompromised SBR. Together with our signal processing pipeline, IT-IF revealed a more complete structural organization of nuclear lamins and enabled detailed quantification of the NL network properties. Beyond the NL study presented here, we expect that our IT-IF method and signal processing platform can be useful in a wide range of nanoscopy applications.

Materials and methods

Cells and viruses

Madin-Darby canine kidney (MDCK) type IIG cells were maintained in low glucose MEM (#41090093, Thermo Fisher Scientific, Gibco™, Paisley, UK) supplemented with 1 % (vol/vol) penicillin-streptomycin antibiotics (#15140122, Thermo Fisher Scientific) and with 10% fetal bovine serum (#10500064, Thermo Fisher Scientific). Cells were maintained under a standard 37 °C and humidified atmosphere with 5 % CO_2, passaged once a week. For the experiments,

cells were seeded for seven days on collagen I (#A1064401, Thermo Fisher Scientific) coated cover glasses (18x18 mm for conventional LSCM, 22x22mm for ExM, high performance, D=0.17 mm, Carl Zeiss Microscopy, NY, USA) prior fixation.

For HSV-1 ExM studies, Vero cells (ATCC) grown on glass coverslips in low-glucose DMEM GlutaMAX (#11570586, Gibco, Thermo Fisher Scientific) to 90 % confluency and inoculated with the virus (HSV-1, MOI 5). The infected and noninfected cells were washed with phosphate-buffered saline (PBS) and fixed with 4 % PFA after 17 h post-infection (pi).

Antibodies

HSV-1 capsids were detected with HSV-1 VP5 MAb (sc-13525, Santa Cruz Biotechnology, Dallas, TX, USA). To detect A-type lamins in this study, mouse monoclonal Abs (mMAbs) against lamin A/C C-terminus residues aa 319-566 (LA/C-C, [131C3], ab1791, Abcam, Cambridge, UK) and lamin A/C N-terminus residues aa 2-29 (LA/C-N, [E-1], sc-376248, Santa Cruz Biotechnology, DA, USA), a rabbit monoclonal Ab (rMAb) against full-length lamin A/C (LA/C-rod, [EP4520-16], ab133256, Abcam), and a rabbit polyclonal Ab (rpAb) against LA/C (exact target sequence declared as proprietary by the manufacturer, ab227176, Abcam) were used. To detect histone H3, a rpAb corresponding to the aa100 of the C-terminus (H3, ab1791, Abcam) was used. RpAb against H3 tail modification at N-terminal aa 1-100 tri-methyl lysine 9 (H3K9me3, Abcam) and anti-actin fluorophore-conjugated phalloidin (ATTO-TEC, NY, USA) were applied in supplemental studies.

Iterative immunostaining

MDCKII cells were fixed with 4 % paraformaldehyde (cat. No. 15713-S, Electron Microscopy Sciences, Hatfield, PA, USA) for 10 min at room temperature (RT), rinsed twice with 1X PBS, and permeabilized for 10 min in RT using 0.5 % Triton X-100 in PBS supplemented with 0.5 % BSA (Bovine Serum Albumin). Iterative immunostaining was begun by incubating the samples with primary Abs diluted in 3 % bovine serum albumin (BSA) for 1h in RT using recommended immunofluorescence labeling working concentrations. Next, the primary Abs (see Table 1) were followed by secondary Alexa 488 and Alexa 568 -conjugated goat anti-mouse and anti-rabbit Abs (1:200 in 3 % BSA/PBS, Thermo Fisher Scientific, Waltham, MA, USA), respectively, for 1h in RT in the dark. This protocol was repeated three times to iterate the Ab treatment and signal intensity. Before each subsequent iteration, the permeabilization step was done using 0.2 % Triton X-100 in PBS supplemented with 0.5 % BSA. After the four iterations, the samples were washed with PBS and deionized water (10 min each) followed by

mounting in ProLong Diamond Antifade Mountant with DAPI (Thermo Fisher Scientific) and led to cure at RT in dark o/n before storing at +4 °C before microscopy. For these experiments n=2-3 replicate experiments containing 5 random image fields with approx. 20 nuclei was used for analyses.

For the expansion of iteratively immunostained samples, a fourfold concentration of secondary Abs was used to retain the signal after expansion. Sample expansion was performed using the previously described proExM protocol for cultured cells (V1.0, REF). After the isotropic expansion, a piece of gel was cut and mounted with 1 % high-melt agarose into an imaging chamber (SC15022, Aireka Cell, Hong Kong, China).

Expansion microscopy

The samples first fixed and stained according to the iterative immunostaining protocol described previously. After the immunolabeling, the samples were incubated in an anchoring solution of 1% 6-((acryloyl)amino) hexanoic acid, succinimidyl ester (#A20770, Acroloyl X-SE, Thermo Fisher Scientific) in PBS for over 6 hours in RT. After the anchoring, the samples were washed with PBS for 2 x 15 mins before proceeding to gelation. Before the gelation, glass coverslips (18mm x 18mm) were prepared to work as a base to cast the gel. A piece of parafilm (P7793, Merck) was glued on top of a coverslip with a drop of cyanoacrylate glue (Loctite Super Glue Power Flex Gel Control, Henkel Norden AB, Bromma, Sweden). The parafilm-coated coverslip was then placed on a 6-well plate lid, parafilm side on top, and the parafilm cover paper was removed. Then, an in-house designed 3D printed spacer was placed on top of the parafilm. The purpose of the spacer is to confine the gel to known dimensions and keep the thickness of the gel as thin as possible. These features will help define the expansion factor and the expansion speed of the gel.

The gelation solution was prepared on ice by adding the inhibitor (4-Hydroxytempo) and the accelerator (TEMED) to the monomer solution. The initiator (APS) was added to the solution just before pipetting it into the opening of the spacer as the solution will gelatinize fast after the inclusion of APS. Thus, it is advisable to prepare the solution into aliquots to separate 1,5ml centrifuge tubes (S1615-5500, Starlab International, Hamburg, Germany) for one to two samples at a time. After adding APS, the solution was vortexed and administered in the middle of the open space in the spacer. Then, the sample was placed carefully on top of the gelling solution sample-side towards the gel. A channel in the spacer ensures that excess gelling

solution will flow out. A metal nut was placed on the constructed gel mold to provide extra weight. The sample was left to polymerize for 30-45 mins in RT.

After the gel had polymerized, the parafilm-coated coverslip was removed carefully. The gel will not stick to the parafilm, and it is straightforward to remove it. A scalpel can be used to trim excess gel from the edges of the gel button. With the sample coverslip still attached, the gel was placed on a clean 6-well plate (#150239, Thermo-Fisher Scientific). Only one sample was placed in one well. It is essential to measure and draw the outlines of the gel button at this time because the gel will start swelling during digestion. It is crucial to know the original size of the gel button when defining the final expansion factor for the sample. We are using custom-made spacers with a well-defined area for the gel button. Thus, it will be the same size every time.

The polymerized gel, together with the sample, was immersed in a 10-fold volume of digestion solution consisting of Tris pH 8.0, EDTA (E5134, Merck), Triton X-100 (T8787, Merck), guanidine HCl (G3272, Merck), and Proteinase K (P8107S, New England Biolabs, Ipswich, USA). The sample was incubated in the solution overnight at room temperature and dark. The gel will detach from the coverslip during incubation or, at the latest, during the first wash with double-distilled water (ddH_2O). The detached gel was moved to a 6-cm dish preserving the orientation of the gel. It is essential to know the side which includes the sample due to the vast size increase of the sample during the next step. The gel was washed with an excess volume of ddH_2O for 1 hour, 3-5 times. The hydrophilic gel will swell during these washes until the expansion reaches a plateau after the third or fourth wash.

Finally, the expanded gel sample was measured for the expansion factor (final dimensions/ original dimensions). The gel was cut with a custom-made puncher, and the resulting gel disc was mounted in a live imaging chamber (Aireka Cells) with low-melt agarose (A7431, Merck). The chamber was filled with ddH_2O to prevent sample shrinkage and drying. For these experiments n=2-3 replicate experiments all containing duplicate gel samples, of which approx. 10 nuclei were imaged from each.

Confocal Microscopy

For LSCM, all samples were prepared as two replicates (n=2) and imaged using constant laser powers and detection voltages, enabling comparable quantitative analysis of the fluorescence intensities. At the confocal microscope, Alexa 488 and Alexa 568 were excited with 488 nm and 561 nm solid-state lasers, respectively. Fluorescence was detected with 525/50 nm and

595/50 band-pass filters. For unexpanded samples, Nikon Apo 60x Oil λS DIC N2, numerical aperture (N.A.) 1.40, the working distance (WD) 0.14 mm was used in imaging, and stacks of 1024x1024 pixels were collected with a pixel size of 0.041-0.052, or 104 nm in the x- and y -directions and 150 nm in the z-direction. For expansion microscopy sample imaging, Nikon CFI Plan Apo IR SR 60x WI, N.A. 1.27, WD 0.17 mm objective was used. Stacks of 1024x1024 pixels were collected with a pixel size of 23.6 nm (103.8 nm/expansion factor 4.4) in the x- and y- directions and 180 nm in the z-direction. The imaging was done using constant laser powers and detection voltages, enabling a comparative analysis of the fluorescent intensity in each channel. Correct laser alignment was ensured by using sub-resolution fluorescent beads (PS-Speck, Thermo Fisher Scientific). Image analysis was done with ImageJ FIJI distribution (Schindelin et al., 2012). For these the n=2 replicate experiments per Ab containing 10 imaging fields with approx. 20 nuclei per image.

Data normalization and analysis of nuclear lamin intensity and colocalization

After imaging, the mean fluorescence intensity of the NL (measured from the total segmented nuclear area) and the background staining intensity (image area omitting the segmented nuclei) were measured. Additionally, detector noise background correction was imaged from similarly mounted samples containing fluorescent beads (from the area omitting the beads). The detector background was then subtracted from the measured values (background correction), and the background-corrected intensity value was normalized to the starting mean intensity value obtained from iteration 1. For Pearson´s correlation coefficient analysis of colocalization in the multicolor experiment, the correct channel alignment was ensured by using sub-resolution fluorescent beads (PS-Speck, Thermo Fisher Scientific). The PCC analysis was done in ImageJ Fiji with the JACoP plugin (Bolte and Cordelieres, 2006). For these experiments the n=2 replicate experiments.

Signal processing pipeline for noise estimation, denoising, and deblurring

In our model for confocal microscopy data, we assume the noise to be additive with signal-dependent variance and spatially correlated (Azzari et al., 2018). The signal-dependent variance models the conversion of light into electric charge and the dark thermal noise. Specifically, the noise variance is an affine function of the signal-expectation (Foi et al., 2008). The noise correlation models the system's optics and the light's diffraction pattern, commonly referred to as point spread function (PSF), after passing through the microscope's lenses (Cole et al., 2011). We model correlated noise as the convolution between a kernel and a white

Gaussian random field. Alternatively, noise correlation can be modeled with the noise power spectral density (PSD), that is the distribution of the noise energy (or variance) in the Fourier domain. Kernel and PSD are related to each other; in particular, the kernel can be calculated as the inverse Fourier transform of the square root of the noise of the PSD. In our noise model, the noise correlation happens before the sensor converts the photons into current; thus, we consider the case of signal-dependent noise post correlation (Azzari et al., 2018)(See Eq. (53). In our processing pipeline we first estimate, modulo a scaling factor, the noise variance function; this is done using the algorithm (Foi et al., 2008). This algorithm is designed for estimating the variance function of signal-dependent white noise and when the noise is spatially correlated (i.e., not white), the algorithm's output is off by a scaling factor that depends on the correlation (Azzari et al., 2018)(See Eq. (68)), which must be estimated separately. To identify this factor, we exploit the fact that the noise spatial correlation does not affect the statistics of an individual pixel (e.g., the variance of a pixel corresponds exactly to a point of the noise variance function). First, we estimate the mean and variance of non-overlapping 1x1x8 windows (i.e., only in the axial direction) of the 3D sequence; we discard the first and last quartiles of the measured variances to remove possible outliers; then we fit a second affine mean-variance function over the remaining points, and we compare the variances from the two affine models at the intensity value of the mean of the observed image: we correct the first function with the ratio between the two values. Next, the noise function is used to apply the generalized Anscombe transform (GAT) (Starck et al., 1998) to our data. The GAT is a variance stabilizing transformation of noisy data that makes the noise variance independent of the signal. In this way, we can estimate the noise PSD using, indiscriminately, the whole stabilized data. For practical reasons it is convenient to estimate the PSD in discrete cosine transform (DCT) domain on a small support 8x8, and then to convert it to the actual noise PSD (Azzari et al., 2018; see Eq. (77)). To estimate the PSD DCT 8x8 we first divide the whole sequence in 3D overlapping 8x8x8 cubes; then, for each cube, we first compute the 2D DCT of each 2D spatial plane, and then we apply, coefficient-wise, the squared median of absolute deviation (multiplied by 1.4826) in the axial direction: in this way we obtain a set of 2D estimates of the 2D noise PSD DCT 8x8, one for each group. Because some estimates might be affected by outliers, we discard some of the estimates. Finally, we estimate the final noise 2D PSD DCT 8x8 by applying the sample median coefficient-wise to all the remaining PSD estimates. Because the noise has been stabilized and a PSD estimate is now available, we can apply any of the many off-the-shelf denoising algorithms developed for correlated additive Gaussian noise to denoise our data.

We denoised the sequence using the framework introduced in (Azzari and Foi, 2016). This approach iteratively filters and refines the estimation in a multi-scale fashion, from coarse to fine scale: at each scale, it first performs binning of the data, and then it applies VST. The resulting signal is corrupted by additive signal-independent correlated noise that can be denoised with any algorithm designed for correlated noise. This iterative approach is well suited for data affected by strong noise (such is the case of expansion microscopy), and it ensures state-of-the-art denoising results. The denoising filter that we use within the framework is the RF3D algorithm designed for videos (3D data) corrupted by correlated noise (Maggioni et al., 2014). It is important to remark that RF3D performs well in challenging cases such as 3D expansion microscopy because it exploits the redundant spatial and temporal information by promoting the sparsity of small 3D spatio-temporal volumes. The software allows the user to also perform deconvolution (deblurring) of the denoised sequence. However, the results reported here have not been deconvolved (n=2 replicate experiments).

SIM

Nikon N-SIM system in Nikon Ti-E inverted microscope body with CFI SR Apochromat100x/1.49 oil immersion objective and Andor iXon Ultra 897 was used for super-resolution SIM imaging. The spherical aberration correction was conducted before every imaging session by using sub-resolution fluorescent beads (PS-Speck, Thermo Fisher Scientific). This was followed by illumination pattern alignment and optimization for the used laser lines (488nm, 561nm, and 640nm). Alexa 488 and Alexa 568 were excited with 488 nm and 561 nm solid-state lasers, respectively. The SIM image reconstruction was conducted in the system by using NIS-elements software. (n=2 replicate experiments each containing 4-10 nuclei)

ExM lamin network analysis

ExM image stacks from the 1x and 4x iterations were used to analyze the stained lamin network coverage. Overall, three areas per sample were analyzed from two samples per iteration. For this purpose, the image stacks were first divided into two sub-stacks, apical and basal. The apical sub stack was used for the final analysis. First, the stack was normalized, and a ridge detection algorithm (Steger, 1998; Wagner et al., 2017) was used to detect string-like lamin A/C structures. The following thresholded image stacks were analyzed by making a maximum intensity projection for area coverage, and by analyzing the network in Avizo 2020.2 (Thermo Fisher Scientific) for nodal and branch length analysis. First, the Auto Skeleton module was

used to extract the centerlines from the network structures. Secondly, the formed graph was analyzed with the Spatial Graph Statistics module. For this analysis, the n=2 each containing 10 nuclei.

Acknowledgements

This work was supported by the Academy of Finland under the award numbers 308315 and 314106 (TOI), 330896 (MVR), 332615 (EM), and the Centre of Excellence in Body-on-Chip Research (312412 (JH)), 336357 (PROFI6 - TAU Imaging Research Platform (LA, MV, AF), and by the Jane and Aatos Erkko Foundation (MVR). University of Jyväskylä Graduate School for Doctoral Studies is acknowledged for the support (SM). The authors acknowledge Biocenter Finland, and Tampere University Tampere Imaging Facility, Virus Production Facility (Title of Docent Eric Dufour), and Flow Cytometry Facility (Dr. Laura Kummola) for their services.

References

Ankam S, Teo BKK, Pohan G, Ho SWL, Lim CK, Yim EKF (2018). Temporal changes in nucleus morphology, lamin A/C and histone methylation during nanotopography-induced neuronal differentiation of stem cells. *Front Bioeng Biotechnol* May 31, 6:69, doi: 10.3389/fbioe.2018.00069.

Azzari L, Borges LR, Foi A. 2018. Modeling and estimation of signal-dependent and correlated noise. In: Denoising of photographic images and video: fundamentals, open challenges and new trendsed (Advances in Computer Vision and Pattern Recognition), ed. M. Bertalmío. Springer International Publishing, doi: 10.1007/978-3-319-96029-6_1, 1–36.

Azzari L, Foi A. 2016. Variance stabilization for noisy+estimate combination in iterative poisson denoising. *IEEE Signal Process Lett* 23:8, 1086–1090, doi: 10.1109/LSP.2016.2580600.

Baines JD. 2011. Herpes simplex virus capsid assembly and DNA packaging: A present and future antiviral drug target. *Trends Microbiol* 19:12, 606–613, doi: 10.1016/j.tim.2011.09.001.

Bolte S, Cordelieres FP. 2006. A guided tour into subcellular colocalization analysis in light microscopy. *J Microscopy* 224:3, 213-232, doi: 10.1111/j.1365-2818.2006.01706.x.

Brueckner L, Zhao PA, van Schaik T, Leemans C, Sima J, Peric-Hupkes D, Gilbert DM, van Steensel B. 2020. Local rewiring of genome–NL interactions by transcription. *EMBO J* 39:6, 1–17, doi: 10.15252/embj.2019103159.

Cavalli G, Misteli T. 2013. Functional implications of genome topology. *Nat Struct Mol Biol* 20:3, 290–299, doi: 10.1038/nsmb.2474.

Chen J, Sasaki H, Lai H, Su Y, Liu J, Wu Y, Zhovmer A, Combs CA, Rey-Suarez I, Chang H-Y, et al. 2021. Three-dimensional residual channel attention networks denoise and sharpen

fluorescence microscopy image volumes. *Nat Methods* 18:6, 678–687, doi: 10.1038/s41592-021-01155-x.

Cole RW, Jinadasa T, Brown CM. 2011. Measuring and interpreting point spread functions to determine confocal microscope resolution and ensure quality control. *Nat Protocols*, 6:12, 1929–1941, doi: 10.1038/nprot.2011.407.

Dahl, KN, Kahn SM, Wilson KL, Discher DE. 2004. The nuclear envelope lamina network has elasticity and a compressibility limit suggestive of a molecular shock absorber. *J Cell Sci* 117:20, 4779–4786, doi: 10.1242/jcs.01357.

Dankovich TM, Rizzoli SO. 2021. Challenges facing quantitative large-scale optical super-resolution, and some simple solutions. *iScience* 24:3, 102134, doi: https://doi.org/10.1016/j.isci.2021.102134.

Dixon JR, Jung I, Selvaraj S, Shen Y, Antosiewicz-Bourget JE, Lee AY, Ye Z, Kim A, Rajagopal N, Xie W, *et al.* 2015. Chromatin architecture reorganization during stem cell differentiation. *Nature* 518:7539, 331–336, doi: 10.1038/nature14222.

Figueiras E, Silvestre OF, Ihalainen TO, Nieder JB. 2019. Phasor-assisted nanoscopy reveals differences in the spatial organization of major NL proteins. *Biochim Biophys Acta Mol Cell Res* 1866:12, 118530, doi: 10.1016/j.bbamcr.2019.118530.

Foi A, Trimeche M, Katkovnik V, Egiazarian K. 2008. Practical poissonian-gaussian noise modeling and fitting for single-image raw-data. *IEEE Trans Image Process* 17:10, 1737–1754, doi: 10.1109/TIP.2008.2001399.

Fortin JP, Hansen KD. 2015. Reconstructing A/B compartments as revealed by Hi-C using long-range correlations in epigenetic data. *Gen Biol* 16:1, 1–23, doi: 10.1186/s13059-015-0741-y.

Gao R, Yu CC (J), Gao L, Piatkevich KD, Neve RL, Munro JB, Upadhyayula S, Boyden ES. 2021. A highly homogeneous polymer composed of tetrahedron-like monomers for high-isotropy expansion microscopy. *Nat Nanotech* 16:6, 698–707, doi: 10.1038/s41565-021-00875-7.

Gaudreau-Lapierre A, Mulatz K, Béïque JC, Trinkle-Mulcahy L. 2021. Expansion microscopy-based imaging of nuclear structures in cultured cells. *STAR Protocols* 2:3, 100630, doi: https://doi.org/10.1016/j.xpro.2021.100630.

Ikoma H, Broxton M, Kudo T, Wetzstein G. 2018. A convex 3D deconvolution algorithm for low photon count fluorescence imaging. *Sci Rep* 8:1, 11489, doi: 10.1038/s41598-018-29768-x.

Laine RF, Albecka A, van de Linde S, Rees EJ, Crump CM, Kaminski CF. 2015. Structural

analysis of herpes simplex virus by optical super-resolution imaging. *Nat Commun* 6:1, 5980, doi: 10.1038/ncomms6980.

Lau L, Lee YL, Sahl SJ, Stearns T, Moerner WE. 2012. STED microscopy with optimized labeling density reveals 9-fold arrangement of a centriole protein. *Biophys J* 102:12, 2926–2935, doi: https://doi.org/10.1016/j.bpj.2012.05.015.

Maggioni M, Sánchez-Monge E, Foi A. 2014. Joint removal of random and fixed-pattern noise through spatiotemporal video filtering', *IEEE Trans Image Process* 23:10, 4282–4296, doi: 10.1109/TIP.2014.2345261.

Newcomb WW, Homa FL, Thomsen DR, Booy FP, Trus BL, Steven AC, Spencer JV, Brown JC. 1996. Assembly of the herpes simplex virus capsid: Characterization of intermediates observed during cell-free capsid formation. *J Mol Biol* 263:3, 432–446, doi: 10.1006/jmbi.1996.0587.

Ojala PM, Sodeik B, Ebersold MW, Kutay U, Helenius A. 2000. Herpes simplex virus type 1 entry into host cells: reconstitution of capsid binding and uncoating at the nuclear pore complex in vitro. *Mol Cell Biol* 20:13, 4922–4931, doi: 10.1128/mcb.20.13.4922-4931.2000.

Pawley JB. 2006. *Handbook Of Biological Confocal Microscopy*, *Handbook Of Biological Confocal Microscopy*, ed. J. B. Pawley, Boston, MA, Springer US, doi: 10.1007/978-0-387-45524-2.

Robson MI, de Las Heras JI, Czapiewski R, Thành PL, Booth DG, Kelly DA, Webb S, Kerr ARW, Schirmer EC. 2016. Tissue-specific gene repositioning by muscle nuclear membrane proteins enhances repression of critical developmental genes during myogenesis. *Mol Cell* 62:6, 834–847, doi: 10.1016/j.molcel.2016.04.035.

Schindelin J, Arganda-Carreras I, Frise E, Kaynig V, Longair M, Pietzsch T, Preibisch S, Rueden C, Saalfeld S, Schmid B. 2012. Fiji: an open-source platform for biological-image analysis. *Nat Methods* 9:7, 676–682; doi: 10.1038/nmeth.2019.

Schirmer EC, Florens L, Guan T, Yates 3rd JR, Gerace L. 2003. Nuclear membrane proteins with potential disease links found by subtractive proteomics. *Science* 301:5638, 1380–1382, doi: 10.1126/science.1088176.

Schnell U, Dijk F, Sjollema KA, Giepmans *BNG.* 2012. Immunolabeling artifacts and the need for live-cell imaging. *Nat Methods* 9:2, 152–158, doi: 10.1038/nmeth.1855.

Starck J-L, Murtagh FD, Bijaoui A. 1998. *Image processing and data analysis: The multiscale approach*. Cambridge, Cambridge University Press, doi: DOI: 10.1017/CBO9780511564352.

Steger C. 1998. An unbiased detector of curvilinear structures. *IEEE Trans Pattern Anal Mach* 20:2, 113–125, doi: 10.1109/34.659930.

Tillberg PW, Chen F, Piatkevich KD, Zhao Y, Yu C-C (J), English BP, Gao L, Martorell A, Suk H-J, Yoshida F. 2016. Protein-retention expansion microscopy of cells and tissues labeled using standard fluorescent proteins and antibodies. *Nat Biotech* 34, 987–992, doi: 10.1038/nbt.3625.

Truckenbrodt S, Maidorn M, Crzan D, Wildhagen H, Kabatas S, Rizzoli SO. 2018. X10 expansion microscopy enables 25-nm resolution on conventional microscopes. *EMBO Rep,* 19:9, e45836, doi: https://doi.org/10.15252/embr.201845836.

Truckenbrodt S, Sommer C, Rizzoli SO, Danzl JG. 2019. A practical guide to optimization in X10 expansion microscopy. *Nat Protocols* 14:3, 832–863, doi: 10.1038/s41596-018-0117-3.

Turgay Y, Eibauer M, Goldman AE, Shimi T, Khayat M, Ben-Harush K, Dubrovsky-Gaupp A, Sapra KT, Goldman RD, Medalia O. 2017. The molecular architecture of lamins in somatic cells. *Nature* 543:7644, 261–264, doi: 10.1038/nature21382.

Wagner T, Hiner M, xraynaud . 2017. 'thorstenwagner/ij-ridgedetection: Ridge Detection 1.4.0', doi: 10.5281/ZENODO.845874.

Wassie AT, Zhao Y, Boyden ES. 2019. 'Expansion microscopy: principles and uses in biological research. *Nat Methods* 16:1, 33–41, doi: 10.1038/s41592-018-0219-4.

Whelan DR, Bell TDM. 2015. Image artifacts in single molecule localization microscopy: Why optimization of sample preparation protocols matters. *Sci Rep* 5, 7924, doi: 10.1038/srep07924.

Figures and Figure Legends

Figure 1.

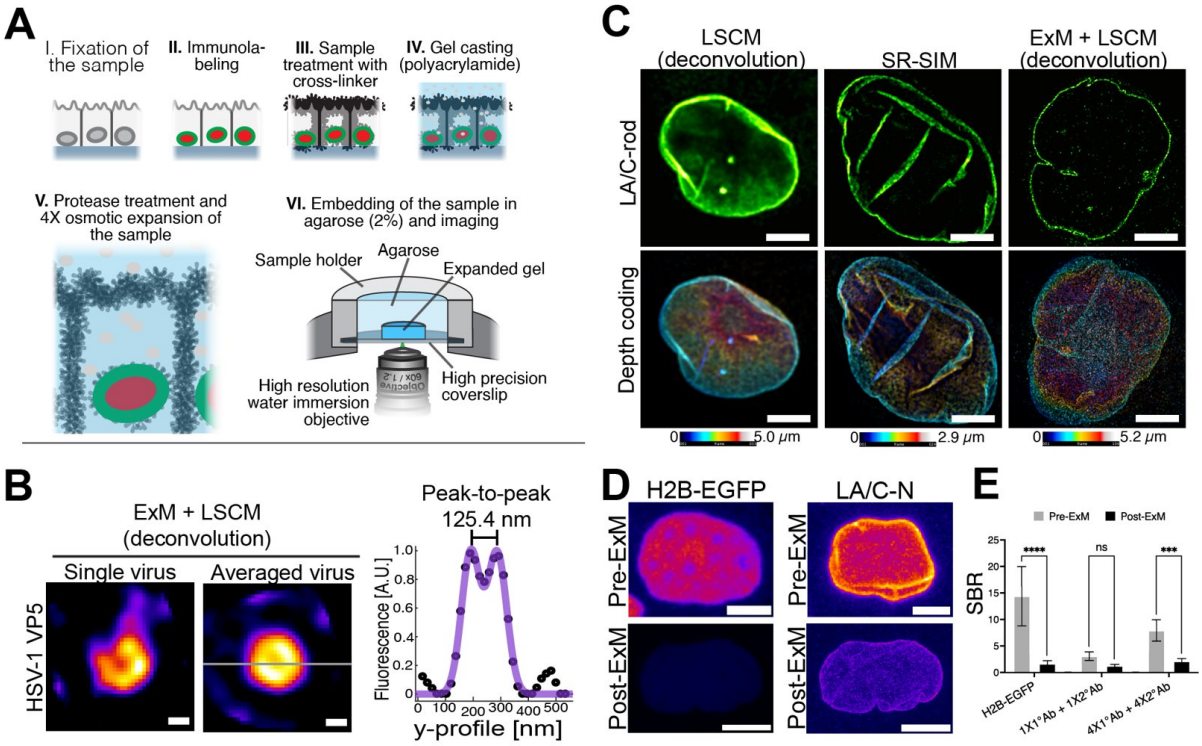

Figure 1. Graphical presentation of pre-expansion microscopy (pre-ExM) sample preparation method and influence of ExM on detection of intranuclear protein complexes and signal fluorescence intensity. (A) Schematics of pre-ExM sample preparation method and imaging setup showing critical steps of sample fixation (i), immunostaining (ii), Acroloyl-X crosslinking (iv), protease treatment followed by the osmotic ~4X expansion (v), and finally, mounting of the gel sample into an IREKA Cell for inverted laser scanning confocal microscopy (LSCM) using a high-resolution water immersion objective (vi). (B) Representative deconvoluted post-ExM confocal microscopy images of intranuclear single (left) and an averaged (n=6; right) viral protein 5 (VP5) Ab -stained HSV-1 capsids and the mean fitted capsid diameter (125.4 nm) measured as a peak-to-peak distance from the fluorescence histogram proving the symmetric expansion of even a complex nuclear protein complex. Scale bars, 40 nm. (C) Deconvoluted LSCM (upper right), super-resolution structured illumination microscopy (SR-SIM) (upper middle), and deconvoluted ExM+LSCM images of an epithelial cell nucleus stained with a rod-domain targeting lamin A/C Ab (Ab) and depth-coded pseudo-color fluorescence intensity maps (lower panels) showing the effect on the detection resolution and proving the power of ExM in imaging of nuclear substructures. Scale bars, 5 µm. (D) Representative pseudo-color fluorescence intensity indicator color

schemed pre-ExM (upper panel) and post-ExM (lower panel) LSCM images of endogenously expressed H2B-EGFP and LA/C-N -stained epithelial cell nuclei showing the decrease in fluorescence intensity after the ExM method. Scale bars, 5µm. (E) Quantification of the signal-to-background ratio (SBR) for H2B-EGFP, and LA/C-N staining before and after ExM with conventional 1X (left two columns) or enhanced 4X (middle two columns) concentrations of both primary (1°) and secondary (2°) Abs after LSCM imaging presenting the decrease in SBR following the ExM method. Columns represent the measured values as a mean ± standard deviation (SD).

Figure 2.

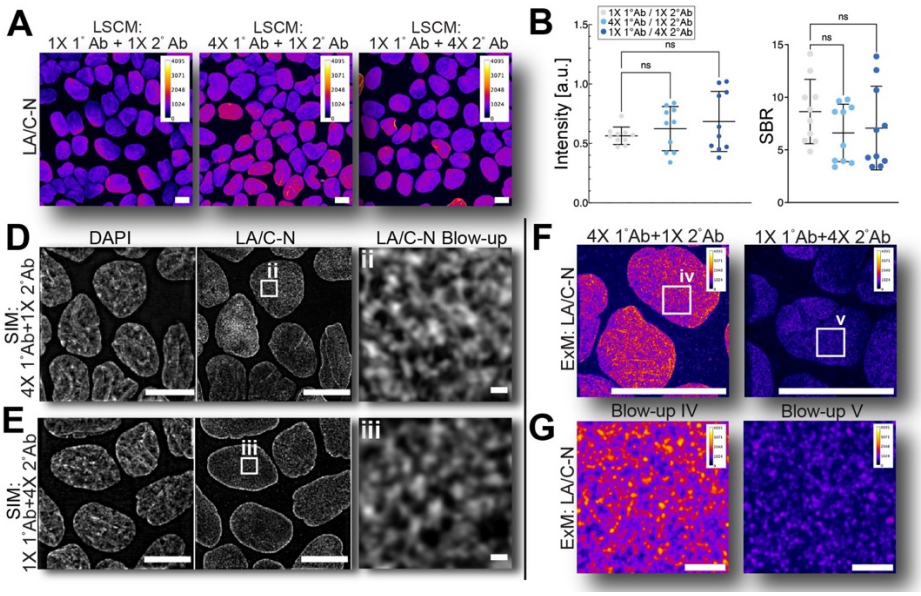

Figure 2. Effects of enhanced primary and secondary Ab concentration on target detection. (A) Representative pseudo-colored intensity indicator color-coded field LSCM images of LA/C-N-stained epithelial nuclei using either conventional 1X primary (1X 1°Ab) with 1X secondary (1X 2°Ab) concentration (left panel), 4-times enhanced primary Ab concentration (4X 1°Ab with 1X 2°Ab, middle panel), or 4-times enhanced secondary Ab concentration (1X 1°Ab with 4X 2°Ab, right panel). Scale bars, 10 µm. (B) Quantification of the mean LA/C-N fluorescence intensity in applied combinations of Ab concentrations (mean ± SD). (C) Quantification of signal-to-background ratio (SBR) in respective conditions (mean ± SD). Structured illumination microscopy (SIM) maximum intensity projection images and their respective blow-ups (ii and iii) of LA/C-N detection using (D) 4-times enhanced primary Ab concentration (4X 1°Ab with 1X 2°Ab, upper panels) and (E) 4-times enhanced secondary Ab concentration (1X 1°Ab with 4X 2°Ab, lower panels). Scale bars, 20 µm; blow-up scale bars, 1 µm. (F) Representative expansion microscopy (ExM) LSCM pseudo-color intensity indicator color-schemed maximum intensity projection images (upper panels; scale bars, 20 µm) and their respective blow-ups (iv and v; lower panels; scale bars, 1 µm) of 4-times enhanced primary Ab concentration (4X 1°Ab with 1X 2°Ab) and (G) 4-times enhanced secondary Ab concentration (1X 1°Ab with 4X 2°Ab). Experimental replicates n=2. Ordinary One-way ANOVA was used to test the statistical significance. Statistically non-significant (ns).

Figure 3.

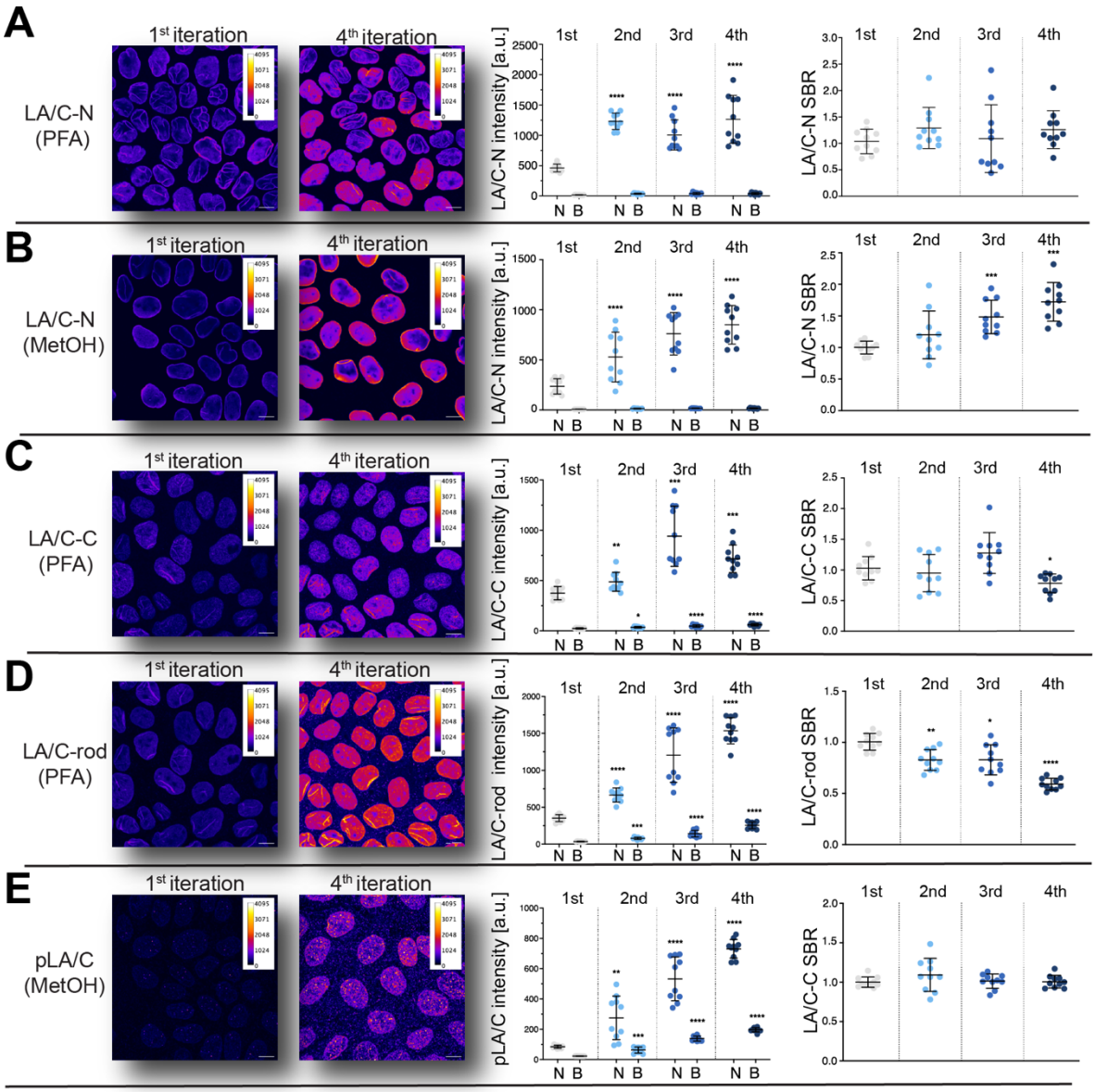

F

	Nuclear fluorescence intensity (mean ± SD)		Background fluorescence intensity (mean ± SD)	
Staining	**1st iteration**	**4th iteration**	**1st iteration**	**4th iteration**
LA/C-N (PFA)	462 ± 64	1264 ± 394	17 ± 4.0	39 ± 16
LA/C-N (MetOH)	236 ± 76	850 ± 193	8 ± 0.4	17 ± 5.0
LA/C-C (PFA)	377 ± 67	716 ± 138	24 ± 6.0	60 ± 12
LA/C-rod (PFA)	352 ± 46	1536 ± 177	34 ± 6.0	255 ± 46
pLA/C (MetOH)	85 ± 10	731 ± 62	23 ± 1.0	197 ± 14

Figure 3. Effect of iterative immunostaining on fluorescence signal intensity and detection quality of nuclear lamins. Representative pseudo-colored intensity indicator color-coded maximum intensity projections of LSCM images acquired after one (far left panels) or four (left panels) iterations i.e., consequent immunostaining cycles, and their respective quantifications of background-corrected mean fluorescence intensity (middle right panels), and

background-corrected signal-to-background ratio (SBR, normalized to iteration 1, far right panels) of (A) LA/C-N on PFA-, (B) LA/C-N on MetOH-, (C) LA/C-C on PFA, (D) LA/C-rod on PFA-, and (E) pLA/C on MetOH-fixed cells. Scale bars, 10 µm. F) Table containing the exact values from the above measurements of nuclear and background fluorescence intensities. Values in plots are presented as a mean ± SD. Experimental replicates n=2. 2way ANOVA with multiple comparisons was used to test the statistical significance. Statistically non-significant (ns) $p>0.05$, *$p<0.05$, **$p<0.01$, ***$p<0.001$, ***$p<0.0001$.

Figure 4.

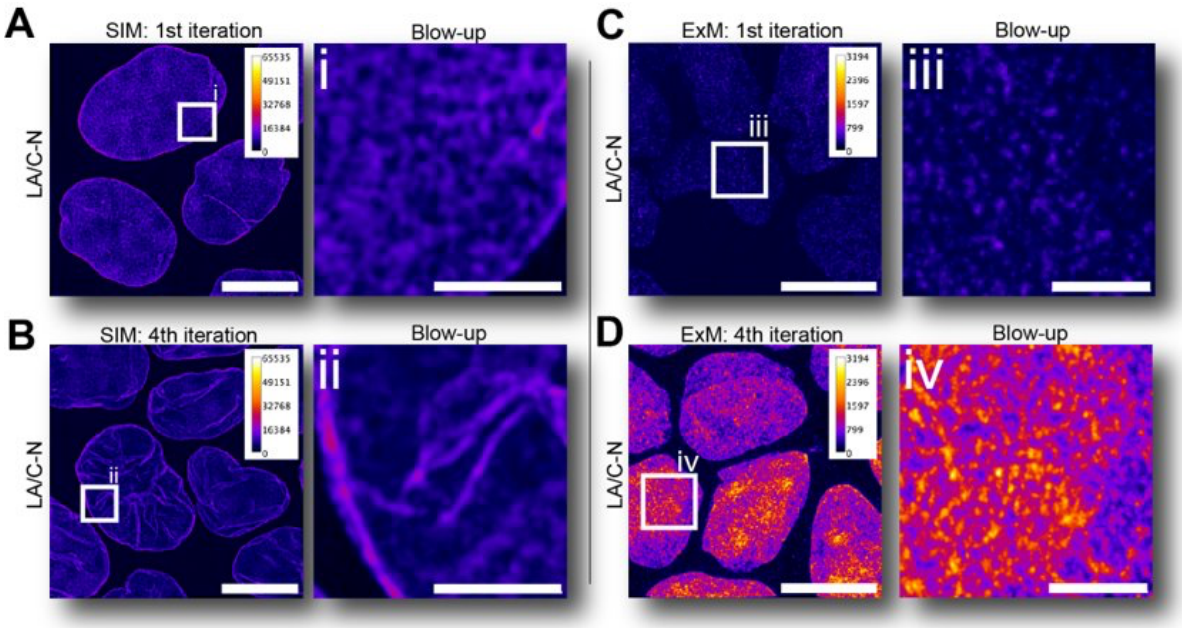

Figure 4. Super-resolution SIM imaging of IT-IF samples. SIM images of representative pseudo-colored intensity indicator color-coded maximum intensity projections and their blow-ups from indicated areas (white box) of (A) first (1st) and (B) four times iterated (4th) LA/C-N staining showing near equal intensities but improved features after 4th iteration. ExM-LSCM images of representative pseudo-colored intensity indicator color-coded maximum intensity projections and their blow-ups from indicated areas (white box) of (C) first (1st) and (D) four times iterated (4th) LA/C-N staining showing increased intensity and staining in the 4th iteration in comparison to those in 1st iteration. Scale bars, 10 µm, blow-up-scale bars, 2 µm), expansion factor of 4.4.

Figure 5.

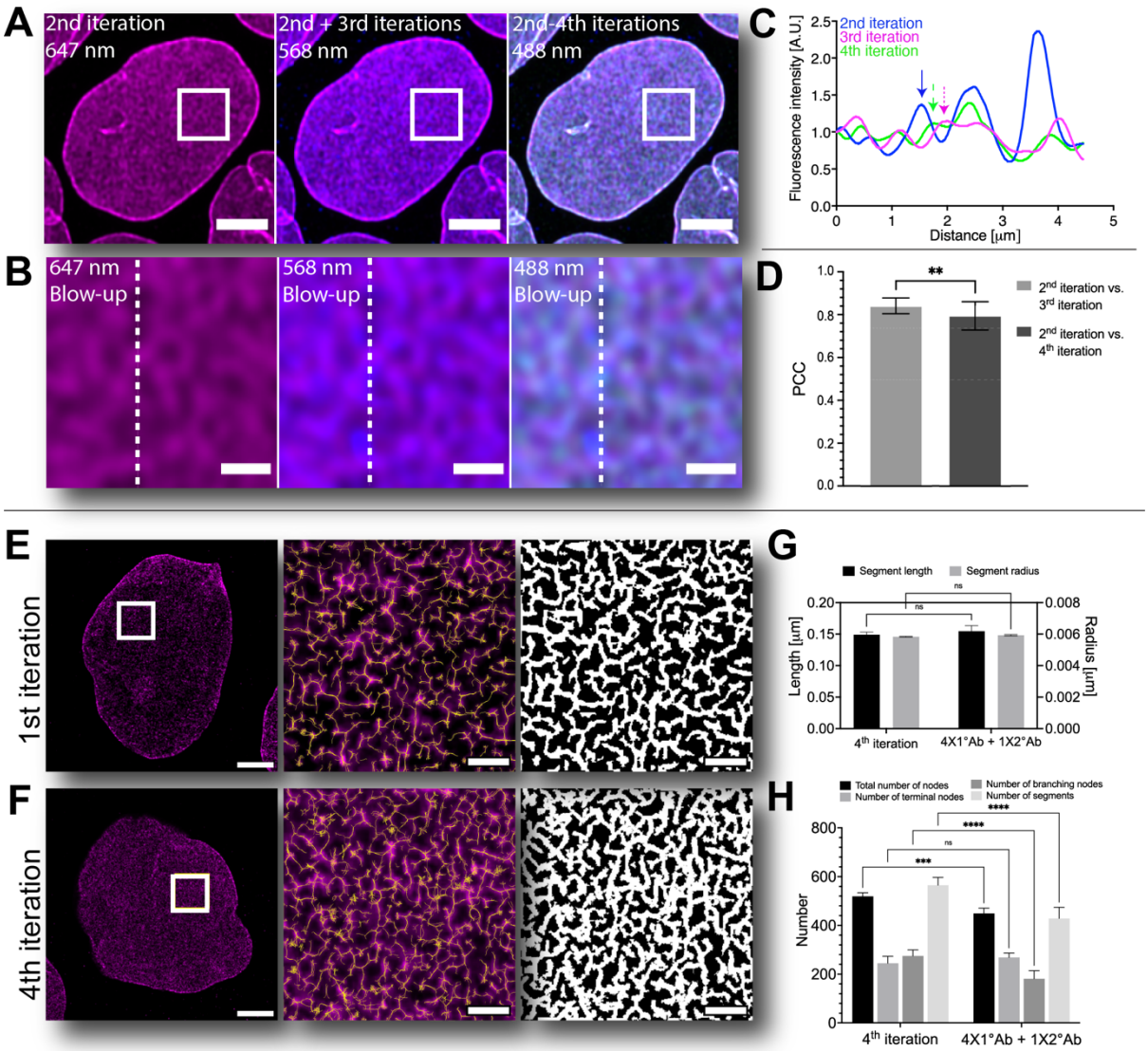

Figure 5. NL network architecture visualized by IT-IF combined with modeling-based denoising. (A) Representative LSCM single optical section images of multicolor analysis of LA/C-N iteration showing detection result after the first two iterations (Alexa 647, upper left panel, magenta), after 3rd (Alexa 568, upper middle panel, blue), and 4th iteration (Alexa 488, upper right panel, green). Scale bars, 5 µm. (B) Blow-ups of indicated areas shown in A. Scale bars, 1 µm. (C) Fluorescence intensity line profile analysis of areas indicated in B, showing the fluorescence intensity distribution of combined 1st and 2nd. (magenta), 3rd (blue) and 4th iterations (green) showing increased Ab binding as iteration-specific intensity peaks. Sources of intensity resulting from unique iterations are represented with distinct arrows with respective colors (magenta: combined 1st and 2nd iterations; blue: 3rd iteration; green: 4th iteration). (D) Quantification of Pearson Correlation Coefficient (PCC) between indicated iterations. **p<0.01, Two-way ANOVA). Representative denoised ExM images of single nuclei showing

(E) ExM optimized LA/C-N staining using 4X 1°Ab/1X 2°Ab concentrations or (F) four times iterated LA/C-N (left panels, scale bars 3 µm), blow-out overlay of indicated areas (white boxes) with calculated network structure (yellow) containing nodes and segments obtained after the image analysis (middle panels, scale bars 500 nm) and reconstructed LA/C-N network (right panels, scale bars 500 nm). (G) Quantification of lamin segment physical properties. (H) Quantification of NL architecture by presenting the number of total, branching, and terminating nodes as well as number of lamin segments within the network coverage. 2way ANOVA was used for statistical testing. Statistically non-significant (ns), p ***p<0.001, ***p<0.0001.